Wearable Multifunctional Bilayer Nanofiber Films for Human Motion Energy Harvesting and Photothermal Therapy

Shaowei Shen, Haoyi Wu, Zihan Xu, Ruirui Cao,* Ying Liu, Yangjiu Zhao, Xin Li, Haoran Yu, Chong Chen,* Xinya Wang, and Caofeng Pan*

In light of the escalating requisites for portability, functionality, comfort, and health in electronic apparatus, the imperative advancement of sophisticated multifunctional textile-based triboelectric nanogenerators (textile-TENGs) is underscored. This research delineates the fabrication of an innovative multifunctional textile-TENG, comprising a photosensitive stratum aimed at thermal regulation and photothermal therapy, alongside a tribo-negative nanofiber film adorning its verso. Exhibiting superlative electrical prowess, the textile-TENG generates remarkably elevated outputs over a wide temperature range, thereby facilitating the efficacious conversion of kinetic energy derived from human motion into electrical energy. Concurrently, the device manifests an exceptional photothermal conversion efficiency, achieving instantly modifiable saturation temperatures (41.52–60.97 °C) under diverse solar exposures, rendering it eminently suitable for a broad spectrum of applications in thermal therapy and regulation domains. Significantly, within cold environments, the textile-TENG demonstrates a capability to augment temperature by approximately 7.4 °C, markedly surpassing conventional cotton textiles in performance. In summation, the textile-TENG is characterized by its unparalleled electromechanical attributes and photothermal conversion efficacies, concurrently facilitating thermal regulation, therapy, and electricity generation. This investigation not only furnishes a referential methodology for the development of advanced multifunctional textile devices but also substantially expands the conceivable application ambit of textile-based technologies.

1. Introduction

The rapid progress of the worldwide economy and the growing consumption of finite resources such as fossil fuels have led to a pressing energy shortage and environmental decline.[1,2] The research and development in energy harvesting devices in this context have become crucial for securing energy needs, achieving recycling, and fostering sustainable economic growth.[3–5] Compared to energy harvesting technologies like solar cells, piezoelectric, and thermoelectric technologies, the triboelectric nanogenerator (TENG) stands out for its exceptional ability to efficiently capture low-frequency and widely distributed mechanical energy and efficiently convert it into precious electrical power.[6–10] This technology shows remarkable promise in terms of its potential for practical applications, sustainability, and widespread accessibility.[11–13] Given that mechanical energy, arising from physical motion, is invariably intertwined with human activities,[14,15] a flexible wearable triboelectric device capable of harvesting ubiquitous and perpetual human motion energy presents an appealing strategy for providing sustainable power.[16,17]

S. Shen, H. Wu, R. Cao, Y. Liu, Y. Zhao, X. Li, H. Yu, C. Chen
Henan Key Laboratory of Photovoltaic Materials
School of Future Technology
Henan University
Kaifeng 475004, China
E-mail: rrcao0403@vip.henu.edu.cn; chongchen@henu.edu.cn
Z. Xu, R. Cao, C. Pan
Institute of Atomic Manufacturing
International Research Institute for Multidisciplinary Science
Beihang University
Beijing 100191, China
E-mail: pancaofeng@buaa.edu.cn

C. Chen
Institute of Solid State Physics
HFIPS
Chinese Academy of Sciences
Hefei 230031, China
X. Wang
College of Textile and Garments
Hebei University of Science and Technology
Textile and Garment Technology Innovation Center of Hebei Province
Shijiazhuang 050018, China

**ADVANCED
SCIENCE NEWS**

www.advancedsciencenews.com

**ADVANCED
FUNCTIONAL
MATERIALS**

www.afm-journal.de

The energy harvesting textiles have emerged as an indispensable power source for a wide range of portable wearable electronic devices, garnering significant attention in the field.[18] Among them, textile-based TENGs (textile-TENGs), which harvests human motion energy, is the focus of current research.[19] With the growing demand for portability, functionality, comfort, and health in electronic devices, it is imperative to develop advanced multifunctional textile-based triboelectric devices.

For textile-TENGs, the comfort and health aspects are of paramount important, in addition to their mechanical energy harvesting performance.[20] It is widely recognized that wearing thick clothing is essential for regulate body temperature and mitigate discomfort or hypothermia in cold environments, which presents a significant challenge for individuals engaged in outdoor work, sports activities, and polar expeditions.[10,21] Therefore, developing lightweight and multifunctional textiles that can achieve localized thermal regulation in the human body is essential for ensuring thermal comfort and health. Meanwhile, the current textile-TENGs lack the therapeutic capabilities and fail to offer timely treatment for health monitoring and intelligent diagnosis.[22]

Photothermal therapy, a physical treatment modality, can be employed for the management of arthritis, congenital hip dysplasia in infants, enhancement of blood circulation, and alleviation of joint stiffness.[22–24] Melanin, a natural pigment renowned for its exceptional light absorption and sunlight protection capabilities.[25] The biocompatible polydopamine (PDA), which shares a structural resemblance to melanin,[19,24] has garnered significant attention in the domains of thermal regulation and photothermal therapy.[26–29] Nevertheless, the exploration of textile-TENGs that integrate thermal comfort and therapeutic performance has never been previously undertaken. Therefore, it is highly necessary to develop multifunctional wearable textile-based devices that possess the capabilities of thermal regulation, thermal therapy, and energy harvesting. Furthermore, these devices have immense practical application value.
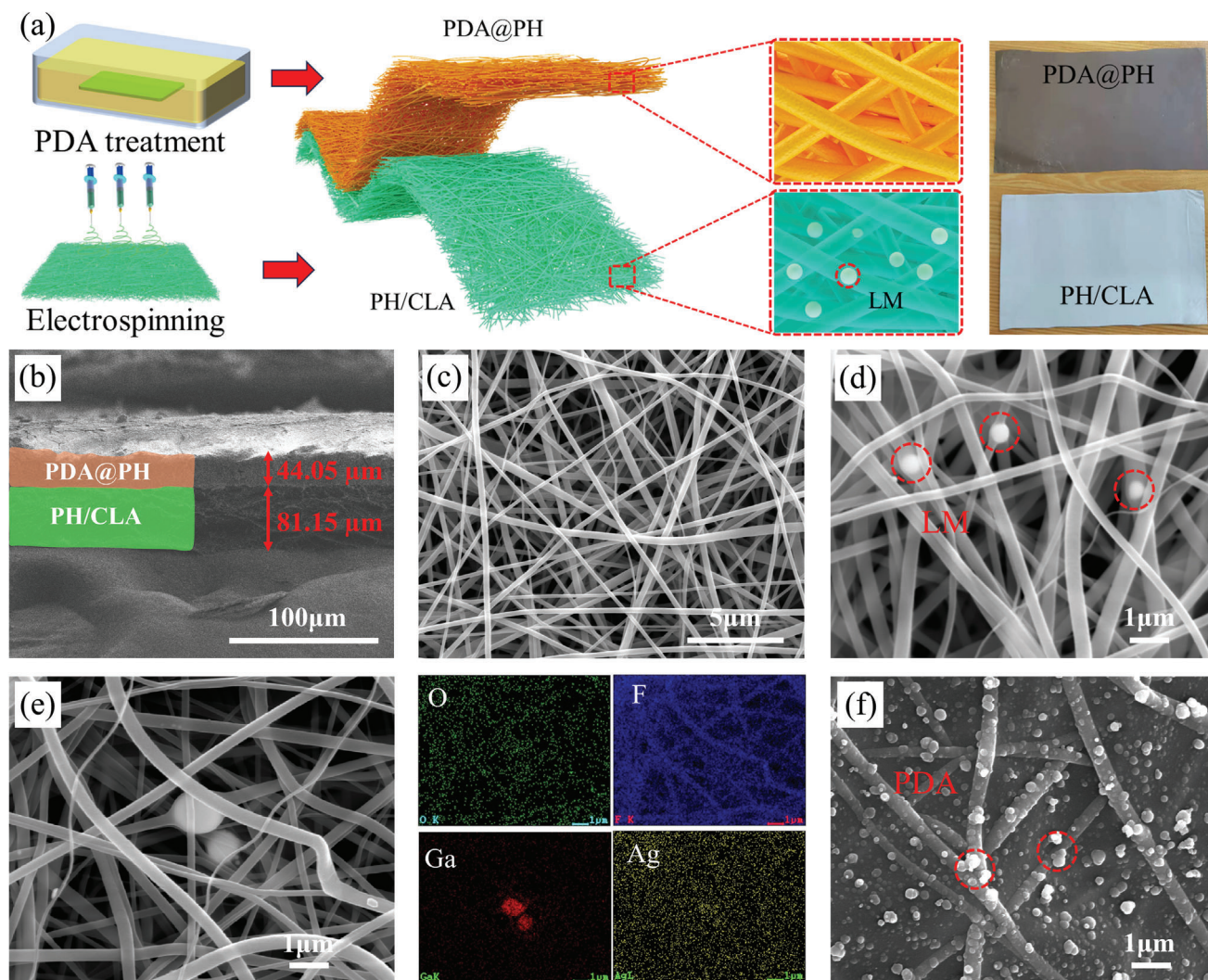
Herein, the multifunctional textile-TENG with a bilayer nanofiber membrane structure, which composed of PDA photosensitive layer for realizing thermal regulation and photothermal therapy and a tribo-negative poly(vinylidene fluoride-*co*-hexafluoropropylene) (PVDF-HFP) nanofiber membrane on the backside, was developed by simple electrospinning and solution impregnation techniques (**Figure 1a**). The textile-TENG with a single-electrode mode demonstrates exceptional electric performance, generating remarkably high outputs (140.62–260.55 V, 0.34–2.40 μA) across various force magnitudes (5–20 N) and frequencies (1.0–4.0 Hz), facilitating efficient harvesting of kinetic energy from human motion energy. Moreover, the multifunctional textile-TENG also exhibits outstanding photothermal conversion performance, creating instantly adjustable saturation temperatures (41.52–60.97 °C) under varying sunlight conditions (50–150 mW cm^{-2}), making it highly promising for a wide range of applications in the fields of thermal therapy and thermal regulation. It is worth noting that wearing this textile based device in cold environments can result in a temperature increase of 7.4 °C compared to conventional cotton textile, which not only reduces energy consumption but also enhances the level of comfort for individuals. In conclusion, this textile-TENG encompasses three simultaneous functions: electricity generation, thermal regula-

tion, and thermal therapy. This study not only provides a reference methodology for the development of advanced multifunctional textile devices but also significantly broadens the potential application domains of textile-based devices.

2. Results and Discussion

As illustrated in Figure 1a, the WMBNF comprises a PDA@PH photosensitive layer and a triboelectric layer consisting of a tribonegative PVDF-HFP/CA/LM/Ag NWs (PH/CLA) nanofiber film, manufactured by a combination of electrospinning and solution impregnation techniques. The optical image in Figure 1a reveals the uniform anchoring of self-polymerized PDA onto the nanofiber film substrate during the process of solution impregnation. The sectional SEM image of WMBNF clearly reveals a distinct bilayer structure, with the photosensitive layer measuring 44.05 μm thickness and the triboelectric layer measuring 81.15 μm, as exhibited Figure 1b. The surface morphology of the pure PVDF-HFP (PH), PVDF-HFP/CA (PH/C), PVDF-HFP/CA/LM (PH/CL), and PH/CLA nanofiber film was depicted in Figure 1c and Figure S1 (Supporting Information), showing a multitude of interconnected nanofiber network structures. In addition, the corresponding average diameters exhibited a gradual increase, measuring 242.7 nm for PH, 275.7 nm for PH/C, 293.0 nm for PH/CL, and 291.9 nm for PH/CLA, as displayed Figure S2 (Supporting Information). As commonly recognized, TENG has seen widespread use in wearable electronic devices,[30–33] Internet of Things,[6,7] environmental sensors,[7,21,34] and medical fields due to its remarkable energy conversion efficiency, cost-effectiveness, and versatility of materials.[31,32,35] The continuous improvement of TENG output performance serves as the driving force for its sustained progress.[36,37] Previous studies have demonstrated that achieving uniform dispersion of fillers within polymer matrices constitutes a pivotal factor in generating excellent triboelectric outputs.[38,39] Therefore, the distribution of fillers in the polymer matrix PVDF-HFP was initially analyzed and investigated through EDS mapping analysis using PH/CLA sample as a representative case, and the corresponding results are depicted in Figure 1e. From Figure 1e, the PH/CLA nanofiber film demonstrates a consistent dispersion of O elements from CA and Ag element from Ag NWs, indicating an even distribution of both fillers within the PVDF-HFP matrix. Furthermore, it is evident from Figure 1d,e that the majority of LM was uniformly encapsulated within polymer nanofibers in the form of small droplets. Additionally, it can be observed from Figure 1f and Figure S3 (Supporting Information) that PDA was successfully polymerized and evenly anchored and coated onto the nanofibers and the gaps between the nanofibers.

The continuous enhancement of TENG's output performance, as previously mentioned, serves as the impetus driving its ongoing advancement.[36,37,40] The inherent characteristics of triboelectric materials determine the output performance of TENG.[41,42] Analyzing the inherent characteristics of triboelectric materials is helpful to explore the origin of output differences between them and deepen the understanding of their underlying mechanism. In particular, the dielectric constant of the triboelectric layer is one of the most important factors, because it is associated with its capability in storing electric charges and is directly proportional to the transferred charge density, which is a

**ADVANCED
SCIENCE NEWS**

www.advancedsciencenews.com

**ADVANCED
FUNCTIONAL
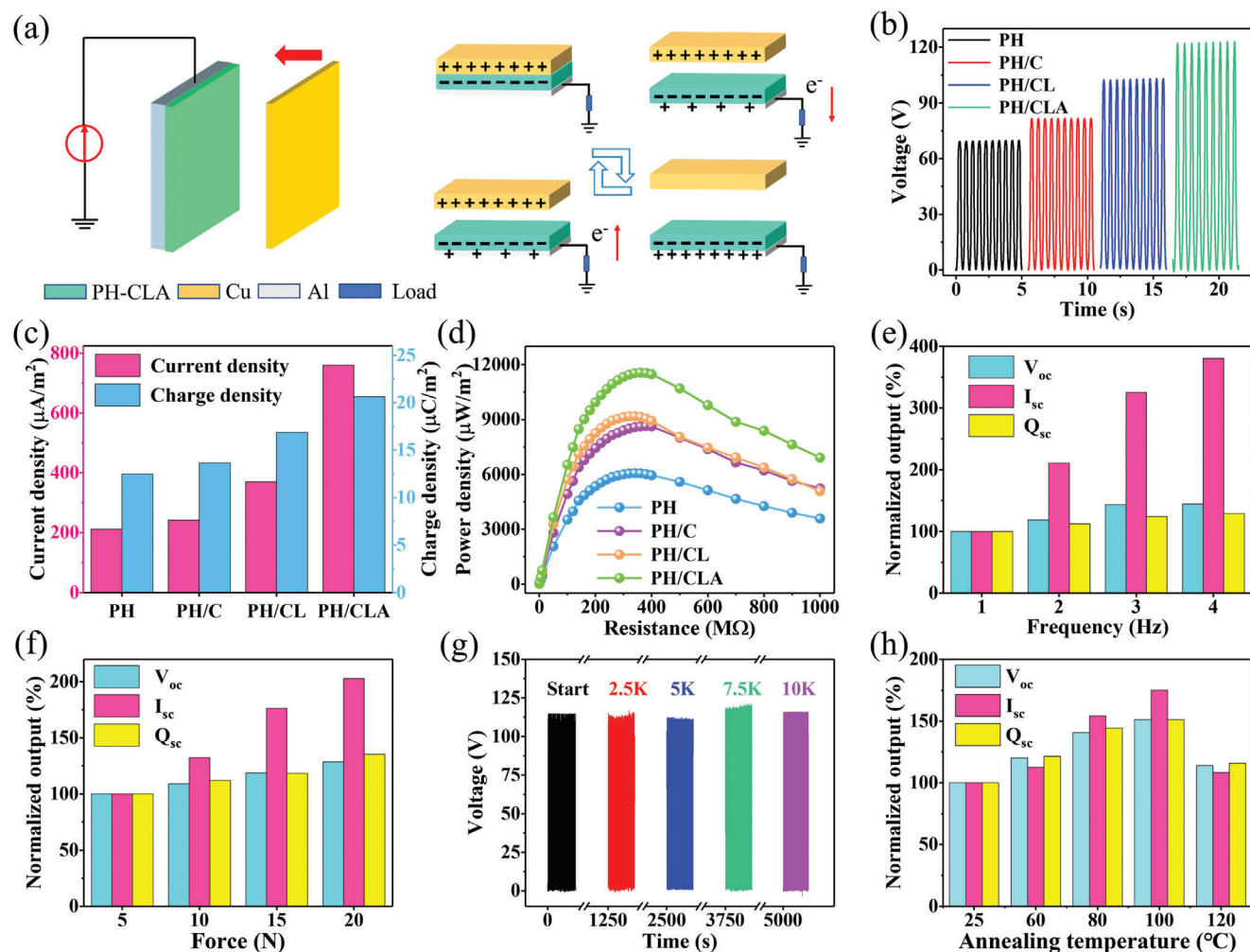MATERIALS**

www.afm-journal.de

Figure 1. a) Schematic diagram and optical photograph of the constructed WMBNF. b) Sectional SEM image of WMBNF. c,d) SEM images of the triboelectric layer in WMBNF at different magnifications. e) SEM and EDS mapping images of the triboelectric layer in WMBNF. f) SEM image of WMBNF photosensitive layer.

decisive factor in the output performance of TENG.[43–45] By modulating dielectric constant, triboelectric surface charge density can be much improved for both surfaces.[46] Therefore, the dielectric enhancement effect is regarded as a promising strategy for augmenting triboelectric performance by appropriately modifying the triboelectric layer.[38] Zheng et al. employed the dielectric enhancement effect to incorporate Ag NWs into the nitrocellulose (NC) triboelectric layer, resulting in a remarkable 360% improvement in the electrical output performance of the NC-Ag NWs based TENG.[38] Previous studies have also demonstrated that the properly incorporation of LM in composite materials leads to enhanced dielectric constants compared to the original polymers, owing to the inherent metallic properties, fluidic nature, and exceptional conductivity of LM.[47,48] However, there is a dearth of research on LM based triboelectric composites.[47,49] Therefore, building upon previous research conducted within our research group,[36] this study further incorporating Ag NWs

and LM into the triboelectric material PVDF-HFP, aiming to further improve the electrical output performance of PVDF-HFP.

First, a series of single-electrode mode TENGs were constructed to investigate the optimal amount of fillers, namely CA, LM, and Ag NWs, in PVDF-HFP. The corresponding device structure and working mechanism are illustrated in **Figure 2a**, and the corresponding electrical output test results were shown in Figures S4–S6 (Supporting Information). From these figures, it can be seen that the optimal amount of fillers in PVDF-HFP, namely CA, LM, and Ag NWs, was 0.5 wt.%, 2 wt.%, and 1 wt.%, respectively. Then, the triboelectric properties of PVDF-HFP composite nanofiber films with the optimal addition amount were compared in this study. Specifically, the effects of adding CA alone, simultaneous addition of CA and LM, and simultaneous addition of CA, LM, and Ag NWs were investigated. The corresponding PVDF-HFP composite nanofiber films were labeled as PH/C, PH/CL, and PH/CLA, respectively, and the

**ADVANCED
SCIENCE NEWS**

www.advancedsciencenews.com

**ADVANCED
FUNCTIONAL
MATERIALS**

www.afm-journal.de

Figure 2. a) Structure schematic diagram and working mechanism of the single-electrode mode textile-TENG. b–d) Electrical outputs of the single-electrode mode textile-TENGs utilizing triboeletric layer PH, PH/C, PH/CL, and PH/CLA, respectively. e) Normalized electrical outputs of the PH/CLA based textile-TENG under a 20 N load at various operating frequencies. f) Normalized electrical outputs of the PH/CLA based textile-TENG under varying loads at 1 Hz operating frequency. g) Durability of the PH/CLA based textile-TENG. h) Normalized electrical outputs of the PH/CLA based textile-TENG at different annealing temperatures.

relevant results are presented in Figure 2b–d. As can be seen from Figure 2b–d, the electrical outputs of the corresponding TENG increases sequentially with the addition of the three fillers. Notably, the PH/CLA based TENG exhibits the highest electrical outputs, reaching values of 122.92 V, 760.49 $\mu A\,m^{-2}$, 20.64 $\mu C\,m^{-2}$, and 11 562.25 $\mu W\,m^{-2}$ respectively, which are found to be 1.77, 3.58, 1.65, and 1.93 times higher than those obtained from PH based TENG. In summary, the triboelectric performance of PH/CLA based TENG has been significantly enhanced, thereby facilitating the continuous advancement of triboelectric devices.

Moreover, Figure 2e,f provides the normalized electrical outputs of PH/CLA based TENG under varying frequencies and loads (specific details can be found in Figures S7 and S8, Supporting Information). As the frequency and compression force increase, both electrical signals exhibit a progressive upward trend. Significantly, the current signal experiences an amplification to 380.8% and 202.9% of its initial value. According to the definition of current intensity as $I = dQ/dt$ (where I represents current in-

tensity, Q denotes transferred charge, and t stands for time), this observed phenomenon could be adequately elucidated.[50] Additionally, as depicted in Figure 2h, this study also investigated the impact of annealing temperature on the output performance of the PH/CLA based TENG for PH/CLA composite film following annealing treatment. It can be observed from Figure 2h that selecting an appropriate annealing temperature can further enhance the electrical output performance of PH/CLA based TENG. Furthermore, the durability of the electrical output performance of the TENG is crucial for continuously advancing the practical application of the triboelectric devices.[51] From Figure 2g, the PH/CLA based TENG demonstrates extraordinary mechanical stability, capable of continuous operation for more than 10 000 cycles without deterioration in output performance, which signifies the exceptional durability of the PH/CLA based TENG, rendering it highly suitable for widespread practical applications.
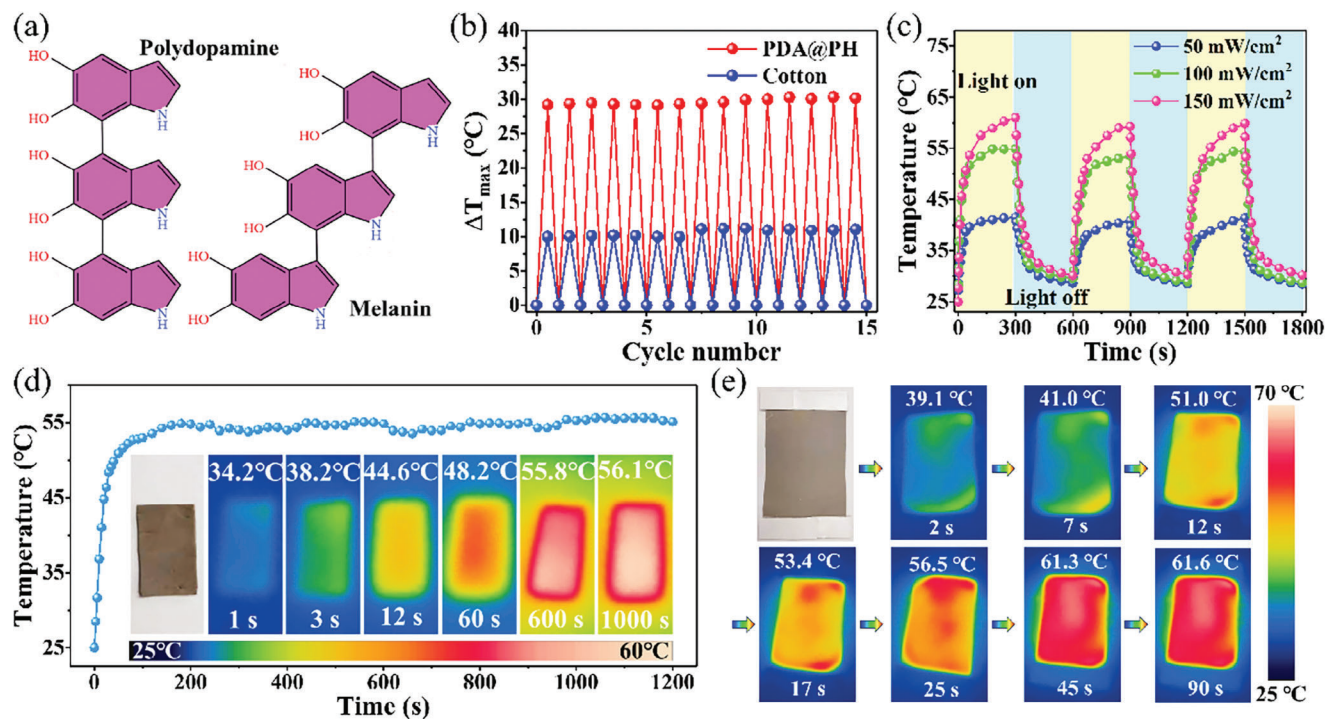
Extensive researches have demonstrated that the intrinsic characteristics of triboelectric materials play a crucial role in
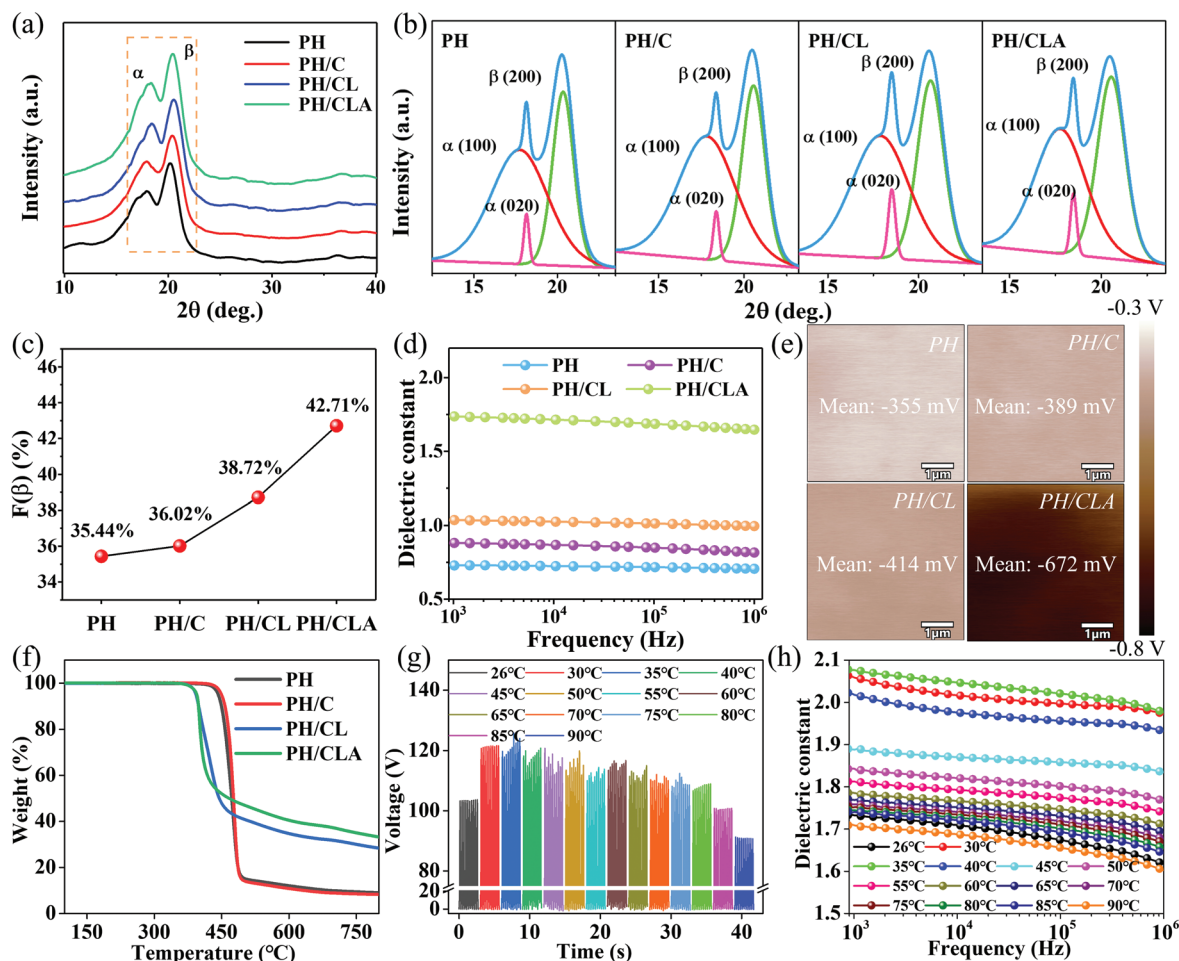
Figure 3. a) XRD patterns of PH, PH/C, PH/CL, PH/CLA nanofiber films, and b) deconvoluted α and β characteristic peaks from the above XRD patterns. c) The β phase content of PH, PH/C, PH/CL, PH/CLA nanofiber films. Relationships d) dielectric constant on the measurement frequency for PH, PH/C, PH/CL, PH/CLA nanofiber films. e) Surface charge potential and f) TGA curves for PH, PH/C, PH/CL, PH/CLA films. g) Electrical outputs and h) relationships dielectric constant on the measurement frequency for PH/CLA nanofiber film under varying temperatures.

determining the output performance of TENG.[36] The PVDF-HFP polymer exhibits three distinct crystal phases: the non-polar α-phase, the electroactive fully polar β-phase, and the semi-polar γ-phase. Among these phases, the β-phase possesses the highest dipole moment per unit cell, resulting in the greatest surface tribo-charge density.[52–54] Consequently, an increased proportion of the β-phase can enhance alignment and polarization of dipoles in PVDF-HFP composite nanofiber films, thereby improving the performance of the corresponding devices. As displayed **Figure 3**a, the crystal phases in the PH, PH/C, PH/CL, and PH/CLA nanofiber films were studied using XRD measurements. The deconvoluted peak of the selected region (2θ = 12°–24°) in Figure 3a is depicted in Figure 3b. The diffraction peaks are observed at 2θ = 17.7°, 18.4°, and 20.7°, corresponding to the reflections of α (100), α (020), and β (110) crystal phase respectively. The calculated results for the content of the β-phase are illustrated in Figure 3c. With successive addition of fillers CA, LM, and Ag NWs into PVDF-HFP, there is a gradual increase in the crystalline content of the β-phase from an initial value of 35.44% (PH) to 36.02% (PH/C), then to 38.72% (PH/CL), ultimately reaching a maximum value of 42.71% (PH/CLA). As

presented Figure S9a,b (Supporting Information), the results of the ATR-FTIR test also confirmed this increasing trend. As previously mentioned, the output performance of TENG devices intricately linked to the surface transfer charge density, which in turn is closely associated with the dielectric properties of triboelectric materials.[55] Subsequently, the surface potential and dielectric properties of the aforementioned four types of nanofiber film samples were characterized, and the relevant results are presented in Figure 3d,e and Figure S9c (Supporting Information). As shown in Figure 3e, the surface charge potential increases negatively from −355 mV (PH) to −672 mV (PH/CLA), which is consistent with the trend of triboelectric output of the aforementioned nanofiber films. Additionally, it is evident that the composite nanofiber films exhibit higher dielectric constants compared to pure PH nanofiber film, as presented in Figure 3d. Notably, the dielectric constant of the composite nanofiber films progressively increases with the addition of three types of fillers. Among them, the PH/CLA nanofiber film has the highest dielectric constant, which is 2.3 times higher than that of the PH nanofiber film, similar to the results obtained from XRD and triboelectric output measurements mentioned above.

ADVANCED
SCIENCE NEWS
www.advancedsciencenews.com

ADVANCED
FUNCTIONAL
MATERIALS
www.afm-journal.de

Figure 4. a) The structure diagram of PDA and melanin. b) Temperature difference (ΔT) of cotton and PDA@PH nanofiber films under solar light irradiation (100 mW cm^{-2}). c) Temperature-time curves of PDA@PH nanofiber film under varying solar intensities. d) Temperature stability of PDA@PH nanofiber film under constant intensity of 100 mW cm^{-2} solar illumination. e) FLIR images of the WMBNF upon solar light irradiation (100 mW cm^{-2}).

Additionally, the dielectric loss of the PH, PH/C, PH/CL, and PH/CLA nanofiber film consistently maintains a low level (< 0.03) across the entire frequency spectrum,[46,56] thereby exerting negligible influence during practical application processes. In summary, with the sequential addition of the aforementioned three fillers, the intrinsic properties of the composite nanofiber membranes (such as dielectric constant, β phase content, surface charge potential, *etc.*) gradually improve, resulting in a significant enhancement of triboelectric performance.

Generally speaking, under high temperature conditions, polymer based triboelectric nanogenerators (PTM-TENGs) struggle to maintain effective electrical output due to the thermionic emission from triboelectric charge and the degradation of PTM mechanical stability.[2,36,57,58] In other words, the electrical output of PTM-TENGs inevitably decreases in high temperature environments, and achieving efficient and stable output under such conditions is crucial for their large-scale application globally.[43,59,60] Notably, the as-fabricated PH/CLA nanofiber film is such a triboelectric matrix that exhibits excellent thermal stability and enhanced triboelectric output over a wide temperature range. As shown in Figure 3f, the initial thermal decomposition temperatures of the above four nanofiber films involved in this study exceed 350 °C, fully meeting the stringent requirements of high-temperature applications. As illustrated in Figure 3g and Figure S10 (Supporting Information), the PH/CLA based TENG exhibits enhanced electrical output between room temperature and 80 °C, which is consistent with our previous research findings,[36,38] ensuring the efficient and stable operation of this textile based TENG device over a wide temperature range. Furthermore, Figure 3h demonstrates that the trend in the di-

electric constant of the PH/CLA nanofiber film with temperature changes is highly consistent with the trend in its triboelectric output performance, revealing the intrinsic reason for its high performance over a wide temperature range.

Melanin, a naturally occurring pigment renowned for its strong light absorption and photoprotective properties, renders it highly suitable for photothermal therapy.[26–28] As depicted in **Figure 4**a, PDA, due to its structural resemblance to melanin,[25] possesses excellent biocompatibility and has garnered significant attention in the field of photothermal conversion and thermal therapy.[61–63] Therefore, this study conducted an extensive investigation into the photothermal conversion characteristics of the prepared PDA@PH photosensitive layer. As displayed in Figure 4b, under sunlight irradiation, the temperature of PDA@PH photosensitive layer rapidly increases with a temperature difference of approximately 30 °C, which is 4 times higher than that observed in the comparative sample (cotton fabric). Figure 4c illustrates the temperature-time curves of PDA@PH photosensitive layer under varying solar intensities, demonstrating the ability to finely tune the photosensitive layer's temperature by adjusting illumination intensity. This means that in practical applications, the PDA@PH nanofiber film can readily and swiftly achieve the desired constant temperature by modulating the illumination intensity.[64] Additionally, the consistent heating rates and saturation temperatures observed during repeated cycles highlight the exceptional durability of PDA@PH, thus facilitating its practical implementation in subsequent textile device studies. Furthermore, Figure 4d presents the responding temperature-time curve and FLIR images of PDA@PH nanofiber film upon solar light irradiation, providing a visually
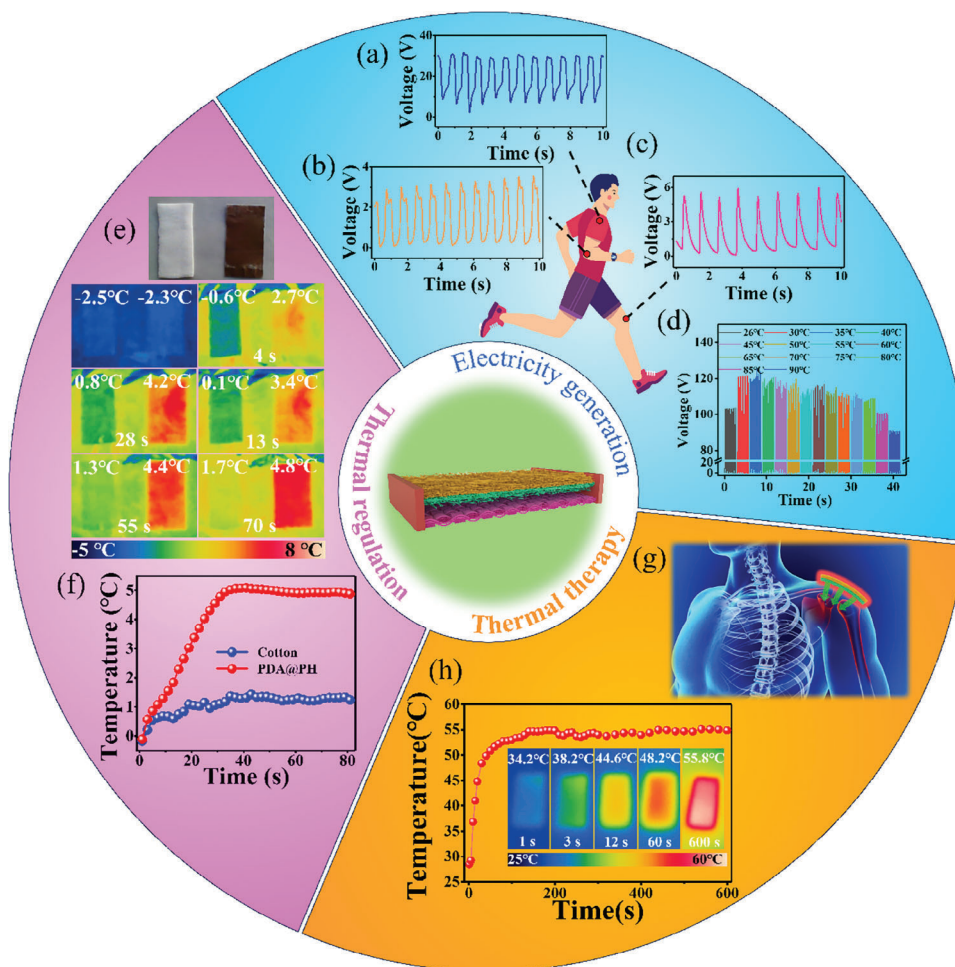
Figure 5. a–c) Response electrical signals of different parts of the human body during movement. d) Electrical outputs of the PH/CLA based textile-TENG at different temperatures. e) FLIR images and f) temperature-time curves of WMBNF and commercial cotton fabric in cold environment (natural sunlight intensity of about 30 mW cm^{-2}). g) The concept map of thermal therapy. h) Temperature-time curves and FLIR images of the WMBNF upon solar light irradiation (100 mW cm^{-2}).

intuitive representation of its long-term photothermal heating performance. The PDA@PH nanofiber film can reach saturation temperature within a few tens of seconds and maintain stability within 1200 s, demonstrating the reliability and durability of the PDA@PH film as a dependable electric-free heating device.

Subsequently, the photothermal conversion performance of the WMBNF constructed in this study was investigated (Figure 4e). Upon exposure to solar irradiation at 100 mW cm^{-2}, the temperature of the constructed WMBNF exhibited a rapid increase and reached a saturation temperature of approximately 61 °C within 90 s. Notably, this saturation temperature aligns with that used for wax therapy in treating developmental dysplasia of the hip in infants. In addition, as shown in Figure S11 (Supporting Information), the WMBNF also exhibits excellent breathability, moisture permeability, and biocompatibility, ensuring user comfort when applied as a wearable electronic device on the human body. Therefore, the WMBNF based textile not only enables thermal regulation for achieving human thermal comfort in cold environments but also facilitates photothermal treatment for developmental dysplasia of the hip in infants. Com-

pared to conventional wax therapy, utilizing this device for photothermal treatment offers significant advantages in terms of enhancing infant comfort during the treatment process. Moreover, the WMBNF photothermal therapy technology can also be applied to potential applications such as arthritis treatment, blood circulation promotion, and joint stiffness alleviation.

The exceptional electromechanical properties and photothermal conversion characteristics of WMBNF textiles have led to the design of a WMBNF textile-based triboelectric device (textile-TENG), which can simultaneously achieve thermal regulation, thermal therapy, and electricity generation functions. The experimental results depicted in **Figures** 5a–d and S12 (Supporting Information) have substantiated the capability of the constructed textile-TENG device to harness biomechanical energy from diverse body movements, while exhibiting efficient electrical output across abroad temperature spectrum. Meanwhile, as depicted in Figure 5e,f, the textile-TENG device exhibits the capability to elevate temperature by 7.4 °C when employed in cold environments, surpassing conventional cotton textiles significantly. This highlights its extraordinary thermal regulation characteristics in

practical applications, not only reducing energy consumption but also enhancing personal comfort. Benefitting of the excellent photothermal conversion characteristics and adjustable saturation temperature of WMBNF, as displayed in Figure 5g,h, this textile-TENG device demonstrates tremendous potential for application in the field of thermal therapy. Therefore, the textile-TENG has tremendous potential in the realm of energy harvesting and self-powered wearable multifunctional electronic devices, even when subjected to adverse environmental conditions.

3. Conclusion

In this study, the multifunctional textile-TENG with a bilayer nanofiber membrane structure, which composed of PDA@PH photosensitive layer for realizing thermal regulation and thermal therapy and a tribo-negative PH/CLA nanofiber film on the backside. Thereinto, the PH/CLA based TENG exhibits the highest electrical outputs, reaching values of 122.92 V, 760.49 μA m^{-2}, 20.64 μC m^{-2}, and 11 562.25 μW m^{-2} respectively, which are found to be 1.77, 3.58, 1.65, and 1.93 times higher than those obtained from original PH based TENG. Moreover, the multifunctional textile-TENG also exhibits outstanding photothermal conversion performance, creating instantly adjustable saturation temperatures (41.52–60.97 °C) under varying sunlight conditions (50–150 mW cm^{-2}), making it highly promising for a wide range of applications in the fields of thermal therapy and thermal regulation. Notably, the textile-TENG device exhibits the capability to elevate temperature by 7.4 °C when employed in cold environments, surpassing conventional cotton textiles significantly. In conclusion, the textile-TENG showcases outstanding electromechanical properties and efficient photothermal conversion capabilities, enabling simultaneous realization of thermal regulation, thermal therapy, and electricity generation functionalities. This study not only establishes a framework for advancing sophisticated multifunctional textile devices but also significantly broadens the potential application domains of textile-based devices.

4. Experimental Section

Materials: PVDF-HFP (Kynar 2500, n_{VDF}:n_{HFP} ≈ 82:18), *N, N*-Dimethylformamide (DMF, 99.5%), dopamine hydrochloride (98%), Tris(hydroxymethyl)aminomethane (Tris, ≥99.8%), and *n*-capric acid (CA) were acquired from Aladdin. Liquid metal (LM, Galinstan) and Ag NWs (average diameter: 100 nm, XFJ59, XFNANO) were used as received.

Fabrication of Wearable Multifunctional Bilayer Nanofiber Film (WMBNF): The WMBNF was fabricated through a combination of electrospinning and solution impregnation techniques, as displayed in Figure 1a, encompassing a photosensitive layer of PVDF-HFP (PH) nanofiber film anchored by PDA (PDA@PH) for thermal regulation and photothermal therapy, as well as a tribo-negative PH nanofiber film on the backside for mechanical energy harvesting. The details are as follows:

1) The PH nanofiber film was fabricated via three-needle electrospinning technique using a 26 wt.% PVDF-HFP/DMF solution as the spinning solution, while employing a roller as the receiving device. Notably, specific spinning parameters included a voltage of 24 kV, a feed rate of 1 mL h^{-1}, a receiving distance of 15 cm, and a receiving time of 2 h. Subsequently, the as-fabricated PH nanofiber film was immersed in a mixed solution comprising dopamine hydrochloride (0.53 mmol), Tris (1.20 mmol), and ionized water (100 mL). Tris buffer was continuously added while adjusting the pH of the solution to a range of 8.0–8.5. After incubating for 24 h, the PH nanofiber film was retrieved, thoroughly rinsed with deionized water, and dried at 60 °C in an oven to obtain the PDA@PH photosensitive layer. The detailed instructions on the preparation of the Tris buffer solution can be found in Supporting Information.

2) The tribo-negative PH layer was constructed using the identical spinning parameters as those employed in the aforementioned experiment. Furthermore, in this experimental section, varying concentrations of CA, Ag NWs, and LM were incorporated into the spinning solution to achieve a triboelectric layer exhibiting enhanced electrical output performance. Please refer to Supporting Information for a comprehensive description of the experimental procedures employed in this section. Furthermore, the aforementioned PDA@PH photosensitive layer was served as receiving substrate for constructing the WMBNF.

Characterization: The morphology of the samples was examined using a Gemini SEM 500 emission scanning electron microscope (Zeiss, Germany). The crystal structure (β phase) transformation of triboelectric layer samples was investigated through the utilization of attenuated total reflection-Fourier transform infrared (ATR-FTIR) and X-ray Diffraction (XRD) analysis. The output performance of the constructed textile-TENG (contact area: 4.5 × 4.5 cm^2) were assessed at an operating frequency of 2 Hz using a high-impedance electrometer (Keithley 6514, USA), and the round-trip distance of the textile-TENG (50 mm) was precisely controlled by a linear motor (R-LP3, Nanoinstrument, China). Dielectric spectra of the triboelectric layer was acquired on a dielectric temperature spectrum measuring instrument (TZDM-RT-1000, China) at the frequency range of 10^3–10^6 Hz. Surface potential measurements were conducted using a KPFM-type atomic force microscope (MFP-3D Origin±, USA). It is important to note that due to its high roughness and excellent flexibility, the electrospun nanofiber film cannot be directly used for KPFM testing. In this study, a thin film prepared by the blade coating method using the same component spinning solution was employed for KPFM testing. The photothermal conversion performance of the PDA@PH photosensitive layer was measured by an infrared thermal imager (FLIR, E6-XT, FLIR Systems, Inc., USA) and a multi-channel temperature testing device (IV3000, IVY TECH).

Supporting Information

Supporting Information is available from the Wiley Online Library or from the author.

Conflict of Interest

The authors declare no conflict of interest.

Data Availability Statement

The data that support the findings of this study are available from the corresponding author upon reasonable request.

[1] E. Ravishankar, R. E. Booth, J. A. Hollingsworth, H. Ade, H. Sederoff, J. F. DeCarolis, B. T. O'Connor, *Energy Environ. Sci.* **2022**, *15*, 1659.

[2] R. Cao, Y. Liu, H. Li, Z. Shen, F. Li, X. Jia, C. Chen, R. Liu, C. Luo, W. Yang, R. Bao, C. Pan, *SusMat* **2024**, *4*, e196.

[3] Y. Jia, Y. Pan, C. Wang, C. Liu, C. Shen, C. Pan, Z. Guo, X. Liu, *Nano-Micro Lett.* **2021**, *13*, 201.

[4] X. Ma, C. Wang, R. Wei, J. He, J. Li, X. Liu, F. Huang, S. Ge, J. Tao, Z. Yuan, P. Chen, D. Peng, C. Pan, *ACS Nano* **2022**, *16*, 2789.

[5] W. Wu, X. Han, J. Li, X. Wang, Y. Zhang, Z. Huo, Q. Chen, X. Sun, Z. Xu, Y. Tan, C. Pan, A. Pan, *Adv. Mater.* **2021**, *33*, 2006006.

[6] W. G. Kim, D. W. Kim, I. W. Tcho, J. K. Kim, M. S. Kim, Y. K. Choi, *ACS Nano* **2021**, *15*, 258.

[7] J. Tian, X. Chen, Z. L. Wang, *Nanotechnology* **2020**, *31*, 242001.

[8] Z. L. Wang, *Adv. Energy Mater.* **2020**, *10*, 2000137.

[9] W. Ma, J. Lu, B. Wan, D. Peng, Q. Xu, G. Hu, Y. Peng, C. Pan, Z. L. Wang, *Adv. Mater.* **2020**, *32*, 1905795.

[10] L. Zhu, L. Wang, C. Pan, L. Chen, F. Xue, B. Chen, L. Yang, L. Su, Z. L. Wang, *ACS Nano* **2017**, *11*, 1894.

[11] H. Wang, Y. Yu, X. Yang, S. Wang, J. Ge, Q. Yang, X. Zhou, G. Zheng, K. Dai, X. Dai, Y. Feng, L. B. Huang, W. Feng, *EcoMat.* **2023**, *5*, e12337.

[12] C. Wang, L. Dong, D. Peng, C. Pan, *Adv. Intell. Syst.* **2019**, *1*, 1900090.

[13] K. Zhou, W. Xu, Y. Yu, W. Zhai, Z. Yuan, K. Dai, G. Zheng, L. Mi, C. Pan, C. Liu, C. Shen, *Small* **2021**, *17*, 2100542.

[14] Y. Zhang, Y. Li, K. Li, Y. S. Kwon, T. Tennakoon, C. Wang, K. C. Chan, S. C. Fu, B. Huang, C. Y. H. Chao, *Nano Energy* **2022**, *95*, 106996.

[15] Q. Zhou, S. Deng, A. Gao, B. Wang, J. Lai, J. Pan, L. Huang, C. Pan, G. Meng, F. Xia, *Adv. Funct. Mater.* **2023**, *33*, 2306619.

[16] J. He, R. Zhou, Y. Zhang, W. Gao, T. Chen, W. Mai, C. Pan, *Adv. Funct. Mater.* **2022**, *32*, 2107281.

[17] K. Zhou, Y. Zhao, X. Sun, Z. Yuan, G. Zheng, K. Dai, L. Mi, C. Pan, C. Liu, C. Shen, *Nano Energy* **2020**, *70*, 104546.

[18] W. Gong, C. Hou, J. Zhou, Y. Guo, W. Zhang, Y. Li, Q. Zhang, H. Wang, *Nat. Commun.* **2019**, *10*, 868.

[19] J. Xiong, P. Cui, X. Chen, J. Wang, K. Parida, M. F. Lin, P. S. Lee, *Nat. Commun.* **2018**, *9*, 4280.

[20] C. Fan, Z. Long, Y. Zhang, A. Mensah, H. He, Q. Wei, P. Lv, *Nano Energy* **2023**, *116*, 108842.

[21] Y. Zhao, W. Gao, K. Dai, Z. Yuan, J. Li, W. Zhai, G. Zheng, C. Pan, C. Liu, C. Shen, *Adv. Mater.* **2021**, *33*, 2102332.

[22] M. Chao, P. Di, Y. Yuan, Y. Xu, L. Zhang, P. Wan, *Nano Energy* **2023**, *108*, 108201.

[23] Q. Wang, H. Sheng, Y. Lv, J. Liang, Y. Liu, N. Li, E. Xie, Q. Su, F. Ershad, W. Lan, J. Wang, C. Yu, *Adv. Funct. Mater.* **2022**, *32*, 2111228.

[24] D. Yang, Y. Ni, X. Kong, S. Li, X. Chen, L. Zhang, Z. L. Wang, *ACS Nano* **2021**, *15*, 14653.

[25] C. G. Bailey, M. D. Nothling, L. L. Fillbrook, Y. Vo, J. E. Beves, D. R. McCamey, M. H. Stenzel, *Angew. Chem., Int. Ed.* **2023**, *62*, 202301678.

[26] V. Gujrati, J. Prakash, J. Malekzadeh-Najafabadi, A. Stiel, U. Klemm, G. Mettenleiter, M. Aichler, A. Walch, V. Ntziachristos, *Nat. Commun.* **2019**, *10*, 1114.

[27] Y. Hu, S. Xue, T. Long, P. Lyu, X. Zhang, J. Chen, S. Chen, C. Liu, X. Chen, *Theranostics* **2020**, *10*, 10448.

[28] X. Li, J. Zhou, H. Wu, F. Dai, J. Li, Z. Li, *Molecules* **2022**, *27*, 4563.

[29] W. Zeng, Z. Li, Q. Huang, C. Ding, L. Yang, W. Wang, Z. Shi, Y. Yang, H. Chen, L. Mei, X. Zeng, *Adv. Funct. Mater.* **2023**, *34*, 2307241.

[30] J. C. Yang, J. Mun, S. Y. Kwon, S. Park, Z. Bao, S. Park, *Adv. Mater.* **2019**, *31*, 1904765.

[31] Y. Gao, L. Yu, J. C. Yeo, C. T. Lim, *Adv. Mater.* **2020**, *32*, 1902133.

[32] Y. Zhao, W. Gao, K. Dai, S. Wang, Z. Yuan, J. Li, W. Zhai, G. Zheng, C. Pan, C. Liu, C. Shen, *Adv. Mater.* **2021**, *33*, 2102332.

[33] R. Cao, Y. Xia, J. Wang, X. Jia, C. Jia, S. Zhu, W. Zhang, X. Gao, X. Zhang, *ACS Appl. Mater. Interfaces* **2021**, *13*, 41657.

[34] Z. Ren, Z. Wang, Z. Liu, L. Wang, H. Guo, L. Li, S. Li, X. Chen, W. Tang, Z. L. Wang, *Adv. Energy Mater.* **2020**, *10*, 2001770.

[35] J. Li, Q. Ding, H. Wang, Z. Wu, X. Gui, C. Li, N. Hu, K. Tao, J. Wu, *Nano-Micro Lett.* **2023**, *15*, 105.

[36] S. Shen, Y. Zhao, R. Cao, H. Wu, W. Zhang, Y. Zhu, K. Ren, C. Pan, *Nano Energy* **2023**, *110*, 108347.

[37] X. Chen, *ACS Nano* **2022**, *16*, 1.

[38] Y. Zhao, S. Shen, R. Cao, H. Wu, H. Yu, X. Li, W. Zhang, C. Pan, *Nano Energy* **2023**, *114*, 108654.

[39] Y. Zhang, M. Wu, Q. Zhu, F. Wang, H. Su, H. Li, C. Diao, H. Zheng, Y. Wu, Z. L. Wang, *Adv. Funct. Mater.* **2019**, *29*, 1904259.

[40] L. Lapčinskis, A. Linarts, K. Mālnieks, H. Kim, K. Rubenis, K. Pudzs, K. Smits, A. Kovaļovs, K. Kalniņš, A. Tamm, C. K. Jeong, A. Šutka, *J. Mater. Chem. A* **2021**, *9*, 8984.

[41] G. B. Min, A. Pullanchiyodan, A. S. Dahiya, E. S. Hosseini, D. Xu, D. M. Mulvihill, R. Dahiya, *Nano Energy* **2021**, *90*, 106600.

[42] M. J. Kim, D. Park, M. N. Alam, S. Lee, P. Park, J. Nah, *ACS Nano* **2019**, *13*, 4640.

[43] R. W. Cheng, K. Dong, L. X. Liu, C. Ning, P. F. Chen, X. Peng, D. Liu, Z. L. Wang, *ACS Nano* **2020**, *14*, 15853.

[44] M. T. Rahman, S. S. Rana, M. A. Zahed, S. Lee, E.-S. Yoon, J. Y. Park, *Nano Energy* **2022**, *94*, 106921.

[45] D. Liu, L. L. Zhou, S. N. Cui, Y. K. Gao, S. X. Li, Z. H. Zhao, Z. Y. Yi, H. Y. Zou, Y. J. Fan, J. Wang, Z. L. Wang, *Nat. Commun.* **2022**, *13*, 6019.

[46] X. Zhang, S. Lv, X. Lu, H. Yu, T. Huang, Q. Zhang, M. Zhu, *Nano Energy* **2020**, *75*, 104894.

[47] X. Xu, Y. Xing, Y. Yin, W. Fang, B. Wu, P. Bei, J. Feng, H. Yu, G. Wang, W. Y. Li, *Chem. Eng. J.* **2023**, *466*, 143175.

[48] J. Yang, D. Tang, J. Ao, T. Ghosh, T. V. Neumann, D. Zhang, Y. Piskarev, T. Yu, V. K. Truong, K. Xie, Y. C. Lai, Y. Li, M. D. Dickey, *Adv. Funct. Mater.* **2020**, *30*, 2002611.

[49] Q. Ye, Y. Wu, Y. Qi, L. Shi, S. Huang, L. Zhang, M. Li, W. Li, X. Zeng, H. Wo, X. Wang, S. Dong, S. Ramakrishna, J. Luo, *Nano Energy* **2019**, *61*, 381.

[50] L. Gong, T. Xuan, S. Wang, H. Du, W. Li, *Nano Energy* **2023**, *109*, 108280.

[51] M. Sun, Q. Lu, Z. L. Wang, B. Huang, *Nat. Commun.* **2021**, *12*, 1752.

[52] S. Cheon, H. Kang, H. Kim, Y. Son, J. Y. Lee, H. J. Shin, S. W. Kim, J. H. Cho, *Adv. Funct. Mater.* **2017**, *28*, 1703778.

[53] L. Li, X. Wang, Y. Hu, Z. Li, C. Wang, Z. Zhao, *Adv. Funct. Mater.* **2021**, *32*, 2109949.

[54] S. Im, S. D. Bu, C. K. Jeong, *J. Korean Inst. Electr. Electron. Mater. Eng.* **2022**, *35*, 523.

[55] Z. Song, W. Li, H. Kong, Y. Bao, N. Wang, W. Wang, Y. Ma, Y. He, S. Gan, L. Niu, *Nano Energy* **2022**, *92*, 106759.

[56] T. Bhatta, S. Sharma, K. Shrestha, Y. Shin, S. Seonu, S. Lee, D. Kim, M. Sharifuzzaman, S. M. S. Rana, J. Y. Park, *Adv. Funct. Mater.* **2022**, *32*, 2202145.

[57] M. Chi, S. Zhang, T. Liu, Y. Liu, B. Luo, J. Wang, C. Cai, X. Meng, S. Wang, Q. Duan, S. Nie, *Adv. Funct. Mater.* **2024**, *34*, 2310280.

[58] J. Chu, W. Wu, Y. Wei, Z. L. Wang, X. Chen, L. Zhang, *Adv. Funct. Mater.* **2024**, *34*, 2402520.

**ADVANCED
SCIENCE NEWS**

www.advancedsciencenews.com

**ADVANCED
FUNCTIONAL
MATERIALS**

www.afm-journal.de

[59] J. Hu, Y. Qian, F. Wei, J. Dai, D. Li, G. Zhang, H. Wang, W. Zhang, *Nano Energy* **2024**, *121*, 109229.

[60] J. Zhao, Y. Wang, J. Chen, Y. Wang, C. Hou, Y. Wang, *Nano Energy* **2024**, *131*, 110210.

[61] L. Liu, R. Li, F. Liu, L. Huang, W. Liu, J. Wang, Z. Wu, N. Reddy, W. Cui, Q. Jiang, *ACS Nano* **2023**, *17*, 9600.

[62] D. Wei, M. Weng, M. H. H. Mahmoud, A. Y. Elnaggar, I. H. E. Azab, X. Sheng, M. Huang, Z. M. El-Bahy, J. Huang, *Adv. Compos. Hybrid Mater.* **2022**, *5*, 1910.

[63] H.-Y. Wu, R.-T. Chen, Y.-W. Shao, X.-D. Qi, J.-H. Yang, Y. Wang, *ACS Sustainable Chem. Eng.* **2019**, *7*, 13532.

[64] Y. Shi, Z. Xiang, L. Cai, F. Pan, Y. Dong, X. Zhu, J. Cheng, H. Jiang, W. Lu, *ACS Nano* **2022**, *16*, 7816.